Accepted Manuscript

DIONISIO 3.0: Comprehensive 3D nuclear fuel simulation through PCMI cohesive and PLENUM models

Goldberg Ezequiel, Loza Peralta Matías E, Soba Alejandro

PII: S0022-3115(19)30023-6

DOI: https://doi.org/10.1016/j.jnucmat.2019.06.005

Reference: NUMA 51662

To appear in: *Journal of Nuclear Materials*

Received Date: 7 January 2019

Revised Date: 22 May 2019

Accepted Date: 2 June 2019

Please cite this article as: G. Ezequiel, L.P. Matías E, S. Alejandro, DIONISIO 3.0: Comprehensive 3D nuclear fuel simulation through PCMI cohesive and PLENUM models, *Journal of Nuclear Materials* (2019), doi: https://doi.org/10.1016/j.jnucmat.2019.06.005.

DIONISIO 3.0: comprehensive 3D nuclear fuel simulation through PCMI cohesive and PLENUM models

Goldberg Ezequiel[a,b], Loza Peralta Matías E.[a,b], Soba Alejandro[a,c*]

[a] Sección Códigos y Modelos, Gerencia Ciclo del Combustible Nuclear, Comisión Nacional de Energía Atómica, Buenos Aires, Argentina.

[b] Instituto de Tecnología Sábato, UNSAM-CNEA.

[c] Consejo Nacional de Investigaciones Científicas y Técnicas, Buenos Aires, Argentina.

Abstract

We present a new version of the DIONISIO code, extending its capabilities to three-dimensional domains. Adding to the functionality that divides the rod in a user-defined number of segments, the user can now choose the dimensionality of the domain in which a representative pellet-gap-cladding system is solved. To achieve this, we have developed a new algorithm to simulate the contact between pellet and cladding based in Cohesive Finite Elements, a natural mode to approach this issue. We present our results testing this kind of contact element in order to validate the concept. Alongside the contact algorithm, we have included a model of the plenum domain in three dimensions, treated using an external FEM mesh created ad hoc. DIONISIO reads this mesh adapting it to the specific case to be simulated and solves the energy equation inside the plenum following specific boundary conditions. We compare the new models to selected experiments under irradiation, in normal or accident conditions, for validation, with results showing a high correlation with said experiments.

Key words: PCMI, PLENUM, Cohesive Finite Elements, DIONISIO three-dimensional model.

[*] Corresponding Author: soba@cnea.gov.ar, Avenida General Paz 1499, Centro Atómico Constituyentes, B1650KNA, Partido de General San Martín, Buenos Aires, Argentina.

1. Introduction

1.1 DIONISIO

DIONISIO is a code that simulates most of the main phenomena which take place within a fuel rod during irradiation under normal or accident operation of a nuclear reactor. The code has more than fifty interconnected models coupled in a modular structure, predicting thermo-mechanical and thermo-chemical evolution of a fuel rod, thermo-hydraulic behavior of the coolant channel around the rod, plenum temperature variation, liberation of different species generated in the pellet and released to the free volume in the rod, among other processes that can take place in a nuclear fuel rod as fracture and pellet cladding mechanical interaction (PCMI). The modifications introduced in the 2.0 version of DIONISIO have been described in detail in previous papers [[1]-[4]]. The finite element method is the main numerical tool used to solve the pellet-gap-cladding system. Prior to the incorporation of the models presented here, axial symmetry was assumed, and axisymmetric finite elements were used to discretize the domain [[5], [6]]. This new version of the code allows to choose between a two or three-dimensional geometry of the domain. With the objective of better simulate the phenomena involved in a fuel rod, the rod is partitioned according to user preference. These sections represent portions of the entire rod subjected to different linear power histories, given the nonuniform longitudinal distribution of neutron flux in the reactor and variable boundary conditions. Fig. 1 exhibits an example division of the active portion of a whole fuel rod. In each axial sector representing a given number of pellets, the differential equations (heat, stress, strain) are solved in a representative pellet and the corresponding cladding segment, discretized with hexahedral and pentahedral elements, as shown in Fig. 1c. The discretization of the portion corresponding to the plenum is constructed with the geometry of a generic fuel rod in mind. The last two pellets, the plenum, the upper plug and the cladding corresponding to those zones are taken into consideration, as marked in the upper portion of the rod scheme in Fig. 1a. A generic hexahedral FEM mesh was constructed as shown in Fig. 1b. This mesh is mapped with the fuel measurements of the input case to be simulated, entered by the user.

In every time step, a complete description of the system variables is obtained for each axial section beginning with the local values of linear power and coolant temperature. First of all, the thermohydraulic behavior of the coolant channel is described [1], [6]. In this calculation, the thermochemical changes of the cladding are

analyzed, such as oxide layer growth, changes of phase and hydrogen capture. Secondly, the heat diffusion equation is solved in the pellet-gap-cladding domain considering Dirichlet boundary conditions determined in the previous part. Afterwards, the fission gas release (FGR), swelling and densification, predicted in the time step under the thermal condition are evaluated [7]. After calculating the amount of gas released by each domain of resolution, the gas released in the sector is evaluated and finally, we integrate the solution of each sector in order to obtain the total amount of gas released over the entire rod. The composition of the gas mixture in the gap and its thermal conductivity are calculated in every time step. Then, the general mechanical equilibrium equation is solved considering the forces enacting over the system (thermal expansion, swelling, densification, irradiation growth for zircaloy, viscoplasticity and creep) [1], [5], [6]. If high burnup is reached, several models evaluate the different mechanical and chemical variations in the pellet and couple this part with the rest of the code [3], [4].

In the plenum model (Fig. 1b), the thermal behavior of the accumulated gas is calculated along with the internal rod pressure using the ideal gas law with the total number of gas atoms released, the entire free volume within the rod and the average of gap temperatures in every segment.

The elongation of every individual pellet and the corresponding cladding are added up to obtain the total elongation of the pellet stack and the rod [4].

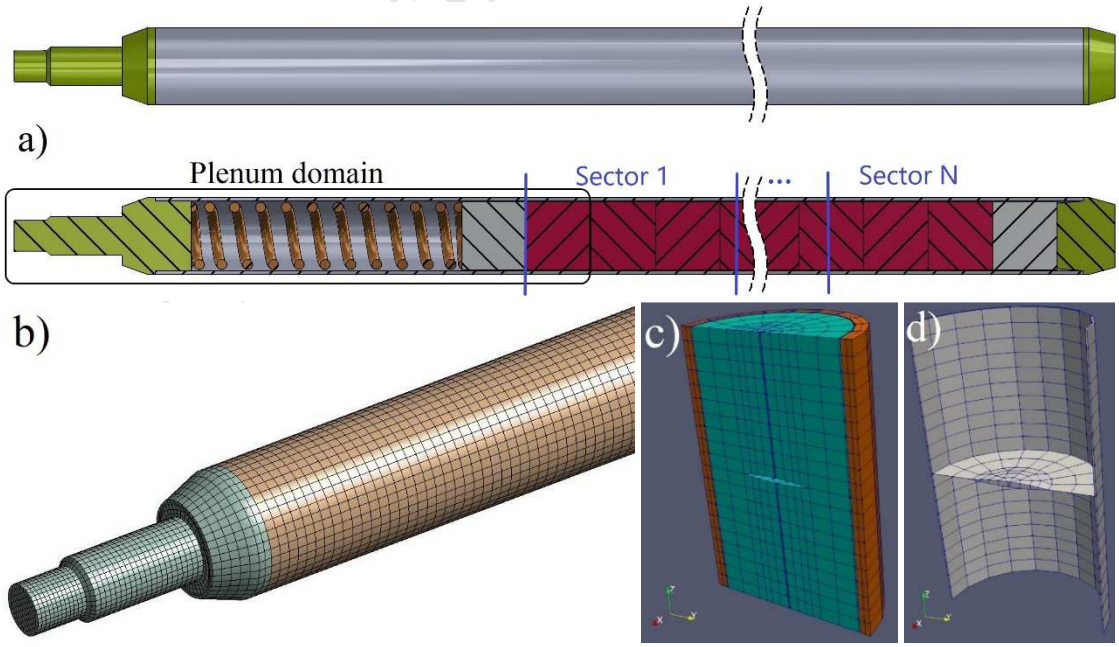

Fig. 1 a) Scheme of the rod showing the plenum, spring, plugs and stack formed by several segments, each one containing a number of pellets. b) Plenum mesh (upper plug in green, rest in brown). c) Two half pellets (green) and cladding (orange). d) Cohesive elements "filling" pellet-cladding and pellet-pellet interfaces.

Given the axial symmetry of the system, neither the geometry nor the surface loading depends on the angular coordinate. Both thermal and hydraulic calculations in the domain are solved considering the *r* and *z* coordinates. The same occurs with the mechanical behavior: displacements, strains and stresses are functions of *r* and *z* only.

Over the material system DIONISIO considers thermal expansion, elastoplastic deformation, creep, densification and swelling (only for the pellet) and irradiation growth (over the Zry cladding) [[1], [4]].

1.2 PCMI in DIONISIO 2D

One of the phenomena that report the greatest mechanical demand for the cladding is the mechanical interaction with the pellet. The interaction is induced by a higher temperature in the pellet with a higher thermal expansion and swelling increase, and the concomitant mechanical interaction of the cladding due to creep by the high external pressure. This phenomenon is relevant in different instances and under different operating conditions. For low burnup and reactors that operate with collapsible sheath, such as CANDU [8], PCMI is crucial from the first instants of irradiation. In PWR/BWR type reactors, the interaction may occur during the last portion of the life in the reactor [9], especially during transient power ramps [10]. PCMI is also pertinent in high burnup (HB) scenarios, in which fuel contains a significant amount of fission gas atoms in the matrix and gas bubble formation induced by thermally activated diffusion of the gas atoms is capable of causing a considerable magnitude of fuel swelling and pellet-cladding mechanical interaction [11]. Similarly, PCMI plays an important role during accident scenarios, especially in RIA, [12] when the short power pulses can cause severe damage through this mechanism.

Besides experimental, theoretical and analytical studies of this phenomena in the past [13]-[19], there is a relatively high and continuous production of relevant investigation on this topic, and new experiments and simulations provide different points of view and alternative solutions. For example, tests are carried out on systems that emulate PCMI conditions, obtaining data of deformation and hoop stress in idealized situations with high control and ease of measurement. In this type of analysis without irradiation, high power ramps are emulated [12], [20], or fuel pods (both Zry and new materials for ATF) are subjected to the typical stress fields of PCMI [21]-[23], obtaining valuable data with which it is feasible to validate models and codes.

On the other hand, many more complex tests, generally carried out under irradiation, from which it is more difficult to obtain detailed measurements in situ, are performed continuously in different facilities [16]-[18], [24]-[27].

Finally, some accident tolerant fuel cladding developments need to consider the kind of requirements to which a fuel will be subjected and analyze PCMI during these conditions by performing experiments or numerical simulations of its behavior [28], [29].

1.3 DIONISIO 3D

There are numerous fuel codes that, among many other physical-chemical phenomena, are devoted to simulating the problem of PCMI. Many of them use axial symmetry in the pellet-gap-cladding domain, treating the rod in different heights to contemplate different points of thermo-mechanical interaction (1.5D [30]-[34] and 2D axisymmetric [35]-[38]). The use of coupled code systems is quite frequent too, using FEM packages to simulate the thermo-mechanical interaction, linking them to fuel codes. Examples of that can be found in several references [9], [33], [35], [38], [39].

In the last years, some full 3D codes have tried to tackle the problem of PCMI without the use of any symmetry. To name a few, FRAPCON-3.4 developed a 3D module dedicated to PCMI simulation [40]; the BISON code works in 3D and treats the interaction explicitly [41].

While it is true that two-dimensional treatments respond to most of the thermo-mechanical effects produced by PCMI, there are certain asymmetries for which these models cannot provide an answer. The eccentricity of the pellet and cladding, the asymmetry in temperature distribution due to the position of a rod in a bundle, especially in accident conditions, or the presence of a defect in the pellet, among others, are situations in which having a full 3D code could deliver results that better represent the experiments than a two-dimensional one.

In this sense, we have developed version 3.0 of DIONISIO, in which we have included a full 3D plenum description (as explained in section 1.1) and a new three-dimensional contact algorithm for the pellet-cladding and the pellet-pellet interfaces. The contact algorithm, directly related to PCMI, is one of the most complex issues to solve in order to move from the 2D axisymmetric version to an entirely three-dimensional domain. In the previous version of DIONISIO we used the Lagrange multipliers algorithm [6] which required the assemble of a variable system adding new

equations when contact occurs. The added contact equations change the system's matrix properties, making it non-diagonally dominant or non-symmetric if rows are swapped (see end of section 2.1 Lagrange multipliers method: axisymmetric system). Besides, the error introduced in the successive iterations until reaching convergence, rendered the problem unstable and expensive from a computational point of view. That is why in the 3D version we have developed an algorithm based on cohesive elements, with a linear contact law that does not alter the system's resolution matrix, making it simpler to solve and easier to parallelize. This method has a notorious disadvantage which is that the problem must be explicitly integrated in time, which is problematic in terms of calculation time involved in comparison to stationary methods [42], [43].

With respect to the three-dimensional plenum model, at the moment it is only thermal due to the low mechanical stress this part of the rod has. The model allowed us to analyze the influence of different parameters on the temperature, such as volume, mesh density, cooling rate and the boundary conditions used. The domain includes the last two pellets of the stack (to evaluate the influence of the high pellet temperature in this specific part of the rod), the Zry cladding and the plug of the same material, the containment spring and the internal gas of the rod. With this system, the plenum temperature variation as a function of the distance to the heat source (the pellets) is studied and the average value is compared to the coolant temperature. The boundary conditions offered to the user can be selected from a variety of options, one of which is the temperature distribution in the plenum (see section 3.2 Boundary conditions).

In this paper, we present a brief description of the cohesive elements method, its calculation advantages and some test results to demonstrate its numerical effectiveness by comparing it with the Lagrange multipliers algorithm in 2D test cases. The three-dimensional test is compared to problems solved by other commercial FEM packages. Additionally, we show the 3D treatments of the plenum, the main assumptions used in the models and some FEM particularities needed for the implementation. Finally, we present the algorithms working in the DIONISIO 3D code reproducing power histories of experiments under irradiation, demonstrating its excellent performance compared with the previous version of DIONISIO and experimental results. The last part of the paper presents some brief conclusions.

2. Numerical treatment of contact problems

2.1 Lagrange multipliers method: axisymmetric system

The PCMI problem in two-dimensional domains in the DIONSIO 2.0 code is treated numerically in the FEM formulation using restriction equations, which do not allow the interpenetration of the surfaces [6]. In each material, an irreducible formulation is applied into the displacement and Lagrange multipliers are used for the treatment of the contact forces over the surface boundaries. The entire formulation is derived from the virtual work principle with the supposition of continuity for the displacement at the frontiers [44]-[46].

The main algorithm used for these simulations is taken from reference [47] in which a general contact formulation is used to simulate problems in plane strain and axial symmetries with or without friction between the domains. At the contact boundary, the surface traction is evaluated from externally applied forces, nodal point equivalent forces (in the virtual works sense) and the magnitude of these tractions is used in the decision of nodal contact or separation. The number of equations is variable, depending on whether contact is present or not [47].

Where contact is produced, force contact is developed between the contactor and the receptor, which are responsible for the elimination of the numeric superposition between the surfaces. These forces are equal in magnitude and have opposite directions; the normal forces are compressive, while tangential forces must satisfy the friction law used. The contact conditions are added to the system of equations in which each node of the receptor boundary has a new contribution to the stiffness matrix for each dimension of the system. In the same way, each contactor boundary node has new components too. As for the independent vector, the new unknows will be the contact forces in each component (see reference [47] for a detailed explanation). In a general problem, the contact forces and the displacements will be in condition of sticking contact, sliding contact or released depending on the coefficient μ between the materials and their separation [47].

Treating the contact using Lagrange multipliers presents some problems regarding the matrix. Firstly, each new contact pair of contactor-receptor nodes adds n-dimension equations to the system. Secondly, these new rows added to the matrix break the properties of the FEM matrixes, i.e.: they are not diagonally dominant anymore; in fact, each new added row has a zero in the diagonal. Then, new solvers based on biconjugate

gradient or similar [48] need to be applied, using row changes to reorder the system to be solved. These inconveniences escalate when a three-dimensional domain is used, where the finite elements in contact become two-dimensional surfaces. Moreover, the Lagrange multipliers method introduces severe difficulties with respect to the directions of the forces, the slips and tension direction in the transversal and longitudinal directions.

2.2 Cohesive Zone Methods (CZM)

In order to overcome these difficulties, we developed a new method, based in the called cohesive finite elements. The Cohesive Zone concept was initially developed to treat discontinuities that evolve within the continuum, such as cracks, and was conceived by Barenblatt (1962) [49], Dugdale (1960) [50], Rice (1968) [51]. These early developments considered the fracture as a gradual phenomenon in which there is a separation between two adjacent virtual surfaces along an extension of the end of the crack (cohesive zone) and is resisted by the presence of cohesive forces. These forces are embodied in tensile-separation laws and link the mechanism of micro structural failure to the deformation field of the continuum. While a conventional crack does not have stress transmission between the corresponding surfaces of the fissure, the "virtual fissure", as it is described by the cohesive zone, is an active field of interactive stress between a pair of virtual surfaces. The fracture process is seen as the progressive decay of the force of the material along adjacent virtual surfaces.

The cohesive tractions between the potential crack surfaces work as resistance to the propagation of the crack. When subjected to external pressures, the atomic structure of the material is modified and reflected as variations in cohesive traction. Up to a certain separation of the virtual surfaces, the cohesive traction follows a growing tendency [52]. After reaching the critical separation, the cohesive traction decreases toward zero. When the tractions between surfaces diminish, the cohesive surfaces separate, defining the formation of a macroscopic fissure. The state of stress between the cohesive surfaces evolves according to a certain softening law of the material, called cohesive law or law of tension-separation. When the cohesive traction decreases to zero, the actual end of the fissure is defined.

Similarly, but in the opposite direction, a real separation between two surfaces can be treated as a virtual separation. The curve defining the traction-separation involves a particular law that has no effect while the surfaces are separated, determines the

moment in which the bodies begin to experience contact and defines the evolution of the contact force in relation to the interpenetration distance [52]. Considering both normal and tangential traction as linear with respect to interpenetration distance, we can calculate them as follows:

$$T_n = \Phi \delta_n \qquad T_t = \Phi \delta_t \mu \tag{1}$$

where Φ is obtained from the Young Modulus of the materials, δ_n represents the interpenetration distance, δ_t is the sliding distance (when in contact) and μ is the friction coefficient between both surfaces. The continuous parts of the material are modeled as usual, by classical constitutive equations, for example, Von Mises plasticity with large deformations [48], [51], [52]. In Fig. 2 and Fig. 3 we use an instructive example [53], [54], [55]] in which a rigid half-spherical shell presses on an elastic semi-space as a consequence of being pushed by a force over the center of the half-space, to provide an illustration of the cohesive elements and the traction-separation law applied. The objective of this problem is to exhibit the cohesive elements between both bodies and their behavior, as intended with the traction law.

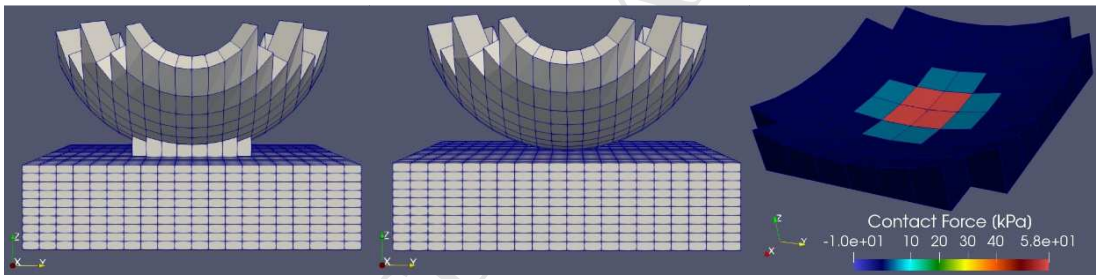

Fig. 2 Example mesh for the Hertz problem. Left: complete mesh. Middle: spherical shell and semi-space elements. Right: cohesive elements, color represents the contact force.

Fig. 2 shows a coarse example of the mesh, with regular finite elements used for the shell and the semi-space and cohesive elements in-between, with color representing the contact force applied by each element. It can be observed that dark blue cohesive elements are not exerting any force given that they are not experiencing contact. This case is only used to explain to the reader how the cohesive elements are meshed and their expected behavior. In Fig. 3 we show the theoretical traction-separation law and the behavior of the contact force of the cohesive elements undergoing contact, with a much finer mesh used, as the problem requires. In b and c, we can see the various contact force magnitudes which depend on the proximity of the element to the center. As can be seen on image c, even though some elements produce contact force while having a positive normal displacement, the value at which traction begins is below 10

µm. This effect is due to integrating the force over an element in which only some nodes are experiencing interpenetration.

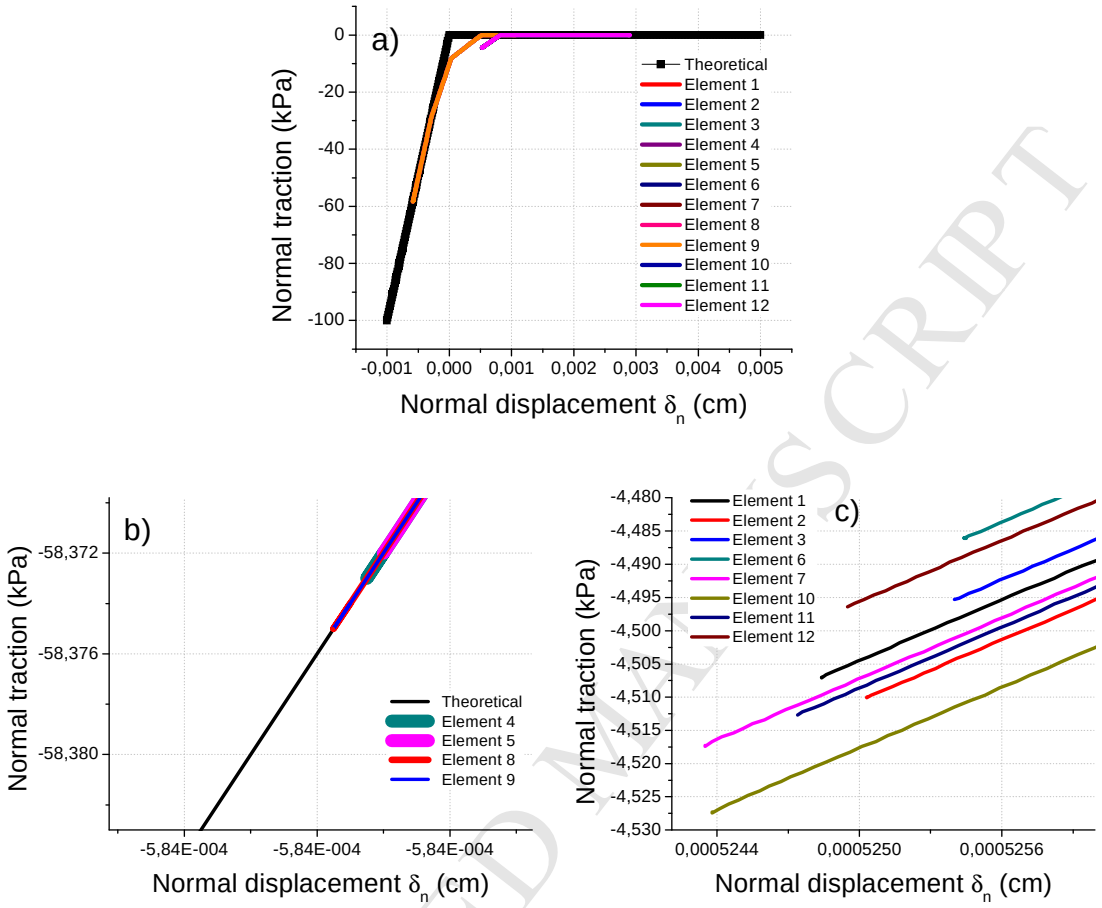

Fig. 3 a) theoretical traction-separation law and cohesive elements results for Hertz problem. b) zoom-in on center elements. c) zoom-in on elements adyacent to the center ones.

As explained above in section 1.1, among the many input parameters of the DIONISIO code, the user can opt to solve a pellet-gap-cladding domain with a half-pellet only or with two half-pellets. We show an example mesh in Fig. 1c, where it can be observed that the half-pellets in green have symmetric dishings with a pellet-cladding gap of 70 microns in that case. In Fig. 1d, we show only the cohesive elements used for the pellet-cladding and pellet-pellet interfaces.

This type of methodology is optimal to be used in the framework of the finite element method. In fact, the founding works of these methods arise from observing the limitations of the FEM itself along with classical theories of mechanical fracture [48], [56]. To this end, variants of the so-called discontinuous Galerkin methods are used, with a generalization of weak formulations, allowing discontinuities of the unknowns within the domain of the problem. To do this, integration is restricted to each sub-domain, naturally generating integral boundary terms for the interfaces that imply jump

discontinuities. It can be observed that the role of these terms is to enforce consistency and continuity of the unknown problem in a weak form, when appropriate [57].

In general, the equations of two bodies in contact can be expressed as follows:

$$\begin{aligned} &\nabla \cdot \sigma + f^{\Omega} = \frac{d^2u}{dt^2} && for\ \Omega \\ &n \cdot \sigma = t && for\ \Gamma_t \\ &u = u_0 && for\ \Gamma_u \\ &n_d^+ \cdot \sigma = t_c^+ \,; n_d^- \cdot \sigma = t_c^- && for\ \Gamma_d \end{aligned} \tag{2}$$

where σ is the stress tensor, u the displacement field and f^{Ω} represents volumetric forces while t represents fixed stresses over the domain or the discontinuity (c). Regarding the domains, Ω stands for the representative volume and Γ for the surface of the volume. In the weak form, the equation is assembled as follows:

$$\int_{\Omega} (\rho_0 \ddot{u} + \bar{\sigma} : \nabla u) d\Omega + \int_{\partial\Omega_c} \|u\| T_c d\Gamma_c = \int_{\Omega} f^{\Omega} \bar{u} d\Omega + \int_{\Gamma} t \bar{u} d\Gamma + R \tag{3}$$

where $\|u\|$ represents the jump in discontinuity $d\Gamma_c = \Gamma_{c+} - \Gamma_{c-}$ and T_c is the stress function of the cohesive element.

This formulation has several characteristics that should be highlighted to clarify concepts:

- It expresses a dynamic equilibrium equation, where the double derivative of the displacement vector in time multiplied by the mass appears in the first integral of the first member of the equation.
- The second integral of the first member is only evaluated for the cohesive elements and adds a term to the system that accounts for the behavior of the discontinuity. The rest of the equation is identical to the one used in the continuous case.
- The analytical T_c function has a variable value, which will depend on the type of physics we wish to treat, whether it is a brittle [58] or ductile [59] material or we are considering large displacements [48], to name some examples. In general, a battery of functions can be found in the literature for this function [51], [52], [57]-[62].

Following the above explanation, cohesive elements in contact problems present us with several advantages over the Lagrange multipliers method: no new equations need to be added to the system and the matrices do not lose any of the properties that they have in the FEM; all modifications to the code are introduced when calculating the local contribution of each cohesive element; no new nodes need to be added to the system, since cohesive elements are formed from already existing nodes on the gap boundaries between cladding and fuel pellet or between two pellet surfaces in contact. Lastly, the CZM provides a natural response in case the contact surfaces are separated after contact, and the contact and separation cycle can be performed as many times as necessary.

It is a given that the method possesses some disadvantages. Firstly, the method possesses severe difficulties for its application in cases where there is large tangential displacement (sliding) between contact surfaces, or the contact pair of element faces is not previously known. In addition, it is required that the meshes on both contact surface match, which might not be suitable for general geometries. As explained in the Introduction, DIONISIO divides the rod in sections and takes a representative pellet for the pellet-gap-cladding system of each sector. The fact that this scenario does not require special studying (as the pellets near the top of the rod would) and the geometry both the pellet and the cladding present, make it a good candidate for the small displacements and small strains consideration, already applied in the previous 2D axisymmetric models, which reduces significantly the possible shortcomings of the method. Another disadvantage of the CZM is the presence of non-physical interpenetration between contact surfaces. Using a dynamic relaxation scheme with pseudo time-stepping (separate from the real time of the power history) provides the possibility to integrate the system explicitly and reach the solution smoothly with the desired precision. On this last point, it is necessary to clarify that any of the intermediate steps is considered unphysical and we only keep the final stationary [42], [43], [59] [63], [64]. This approach results to be more demanding in terms of calculation time compared to stationary methods, but it allows us to achieve small increments in the displacements, which in turn limit the interpenetration to a minimum (less than 3% of the cladding thickness) while remaining stable and ensuring convergence.

While the method might not be suitable in certain circumstances or for certain specific areas of the rod, we have found that for our simulations the disadvantages of the CZM are far outweighed by the advantages over the Lagrange Multipliers approach.

2.3 Test cases

In order to show the reliability of the CZM in the prediction of contact situations, in this section we present and compare results of selected test cases to analytical solutions, finite elements commercial software and experimental results.

2.3.1 Circular Flat Punch

The problem consists of a rigid, flat and circular tip of radius *a* pressing on the surface of an elastic semi-space, under the action of a force *P*. The analytical solutions for this problem are taken from reference [53] where the expressions for displacements and stresses in the infinite semi-plane are presented, in addition to some particular solutions for the surfaces of the half-plane ($z = 0$) and the central axis of symmetry ($r = 0$).

The displacement vector takes the form:

$$2\mu u_r(r,z) = \frac{P}{2\pi a}\left(\frac{rz\sqrt{u}}{a^2 s(1+u)} - \frac{(1-2\nu)a}{r}\left(1 - \frac{z}{a\sqrt{u}}\right)\right)$$

$$2\mu u_r(r,z) = \frac{P}{2\pi a}\left(\frac{z^2}{a^2 s\sqrt{u}} + 2(1-\nu)\tan^{-1}\frac{1}{\sqrt{u}}\right) \tag{4}$$

$$s = \sqrt{\left(({}^{r}/_{a}) + ({}^{z}/_{a})^2 - 1\right)^2 + 4({}^{z}/_{a})^2}$$

$$u = 0.5(({}^{r}/_{a})^2 + ({}^{z}/_{a})^2 - 1 + s)$$

and stresses over the entire domain have the form:

$$\frac{\sigma_{rr}}{pm} = -\frac{1}{2}\left((1-\rho^2)^{-1/2} - (1-2\nu)\frac{1}{\rho^2}\left(1-(1-\rho^2)^{1/2}\right)\right)$$

$$\frac{\sigma_{\theta\theta}}{pm} = -\frac{1}{2}\left(2\nu(1-\rho^2)^{-1/2} + (1-2\nu)\frac{1}{\rho^2}\left(1-(1-\rho^2)^{1/2}\right)\right) \tag{5}$$

$$\frac{\sigma_{zz}}{pm} = -\frac{1}{2}\left((1-\rho^2)^{-1/2}\right)$$

where pm is the average pressure exerted.

In particular, in the center of the contact zone, the radial and tangential stresses are equal, while the stress in *z* is equal to half the average pressure *pm*. The *z* component of stress and displacements take the form:

$$\sigma_{zz}(\rho,0) = -\frac{P}{2\pi a^2}\frac{1}{\sqrt{1-\rho^2}} \qquad \rho < 1 \tag{6}$$

$$u_z(\rho,0) = \frac{1-\nu^2}{\pi E}\frac{P}{a}\sin^{-1}\frac{1}{\rho} \qquad \rho \geq 1$$

The case of a flat tip can be treated in axial symmetry, in which case it will correspond to a problem of circular indentation, or in symmetry of plane strain, in which case it will be a tip of width *a*, infinite in the direction of symmetry.

In Fig. 4 we present the results of the cohesive zone model for radial and axial displacements for the $z = 0$ plane (contact surface) and the axial stress on the $r = 0$ axis (axis of symmetry), compared to the analytical solution and the Lagrange multipliers model. While for the displacement in the axial direction (central figure) both numerical methods produce results with a similar uncertainty range, a better prediction by the CZM for the radial displacement (left figure) is observed, especially in the effective contact surface of both bodies ($r < a$), due to the calculation of tangential forces that are natural within the solution of the model. The errors in the solution corresponding to the Lagrange Multipliers Method are a result of the several penalization parameters applied for every direction that displacements can occur (normal or separation and tangential or sliding), a frequent case when dealing with contact problems with such an approach which is quite difficult to avoid [65].

For similar reasons, the CZM presents results that correspond more with the analytical curve with respect to the stresses (the axial ones are shown in Fig. 4, on the right).

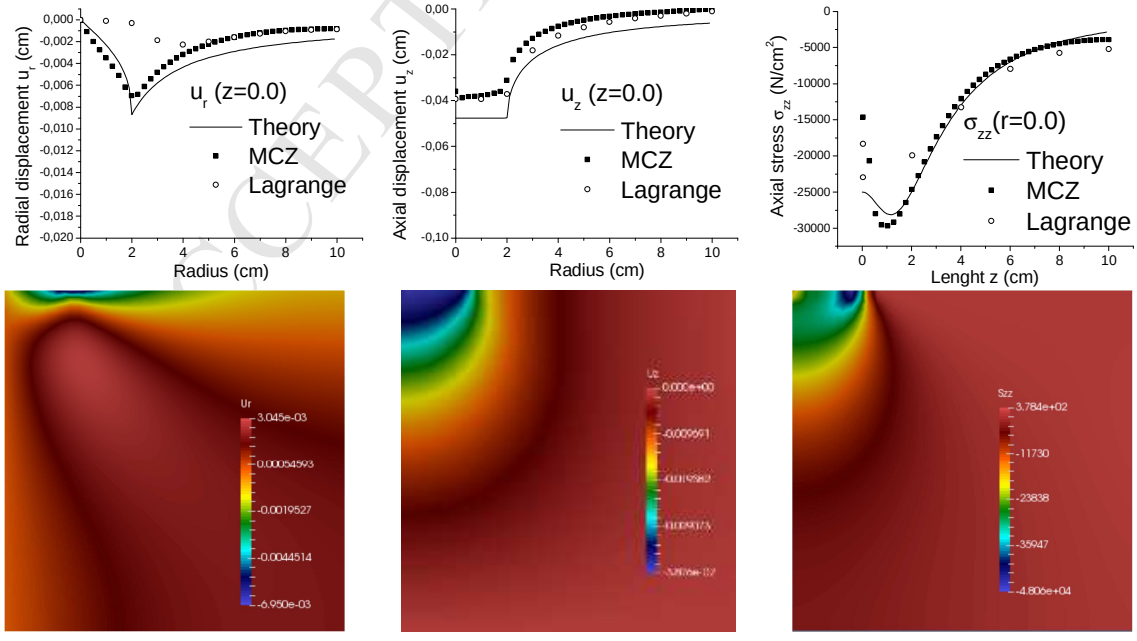

Fig. 4 Left: radial displacements on the contact surface (z=0). Middle: axial displacements on the contact surface (z=0). Right: Axial stress on the axis of symmetry (r=0). The bottom graphs represent the corresponding tensor components extended over the entire domain.

2.3.2 Thermo-mechanical behavior of SiC composite

In reference [22], a nuclear grade silicon carbide fiber (SiC_f) reinforced silicon carbide matrix (SiC_m) composite is studied under a high temperature gradient as a candidate material for accident tolerant fuel cladding. They compare experimental results to a FEM model built using commercial software COMSOL (Stockholm, Sweden). In the experimental setup, a solid surrogate alumina tube is placed within the SiC sample and bonded using a ceramic adhesive. The whole setup is heated from the center thus exerting pressure as a result of the thermal expansion. Given that the aim of our model is to study the mechanical interaction during contact of the surfaces, our model excludes the ceramic adhesive given that it serves as a strain and stress buffer. In Fig. 5, we show the initial and final states regarding displacements and temperature of the sample. Radial displacements have been increased 25 times making them simpler to observe, which causes the interpenetration seen in the image on the right to appear bigger when actual values lie in the range of units of microns (0.5% of cladding thickness).

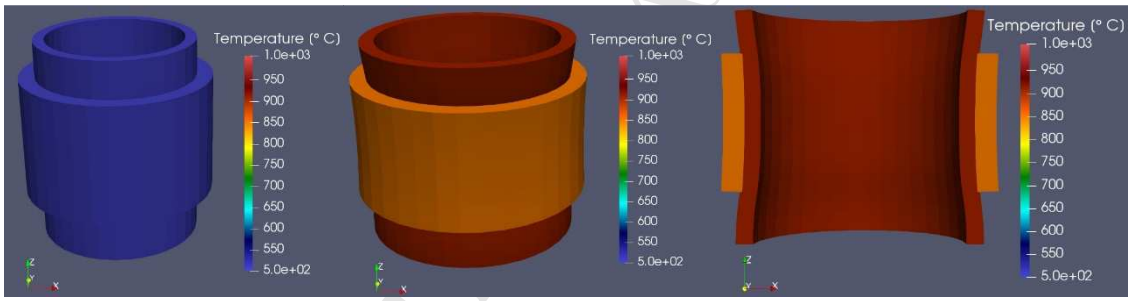

Fig. 5 Left: initial geometry. Middle and Right: final status of the domain (radial displacements x25).

As can be seen in Fig. 6, both the hoop and radial component of mechanical strain and total strain (mechanical plus thermal) correlate very well with the model [22], excluding the bond layer (from 0.9 mm to 1.2 mm from the center), which absorbs most of the radial strain given that it's elasticity modulus is assumed to be 0.05 times that of the alumina surrogate. The stress values along the length of the sample present very similar values as shown in Fig. 7, as do the stress values along the thickness of the setup, with the exception of the step produced by the adhesive.

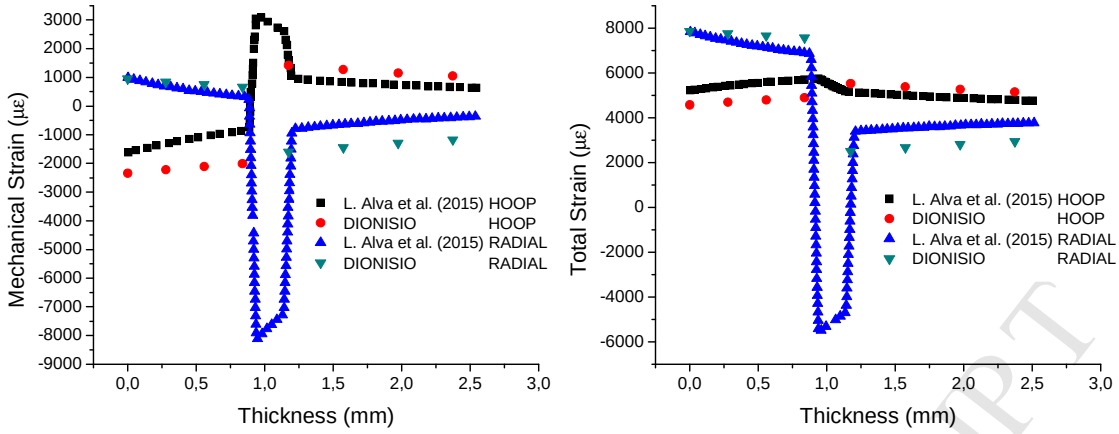

Fig. 6 Hoop and radial strain through the thickness of the sample compared to numerical results [22].

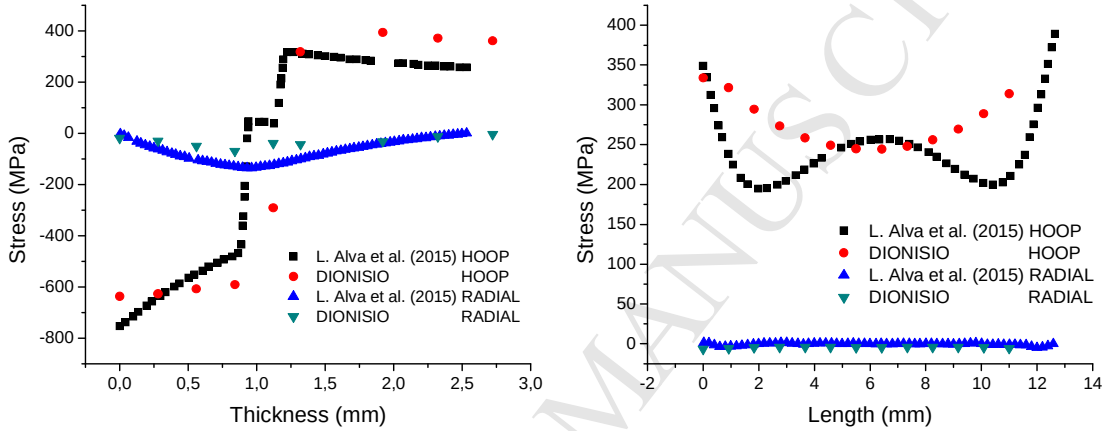

Fig. 7 Hoop and radial stress along the thickness (left) and length (right) of the sample, compared to numerical results [22].

3. Numerical treatment of PLENUM

3.1 Conductivities

As explained in section 1.1, the plenum domain considers the last two pellets of the stack, the Zry cladding and the plug of the same material, the containment spring and the internal gas of the rod, each of which possesses a thermal conductivity. Given this domain, we solved the energy balance equation so as to obtain the temperature distribution, taking into consideration the volumetric power source from the pellets and the heat conduction in all the materials involved.

In addition to depending on the material, the thermal conductivity presents strong nonlinearities with respect to temperature, porosity and burnup. For the UO_2 pellet the following thermal conductivity function is considered [66]:

$$k = \left(1 - p^{2/3}\right)\left[\frac{1}{A + B\,T + C\,T^2 + [a_{Gd} w_{Gd}(b_{Gd} - T)] + h_D(T, Bu)} + (1 - c_{Gd} w_{Gd})\frac{D}{T^{5/2}}\, exp\left(-\frac{E}{T}\right)\right]\left[\frac{W}{cm\ ^\circ C}\right] \quad (7)$$

where p is the porosity, Bu the burnup in MWd/kg$_U$, w_{Gd} is the weight fraction of Gadolinium, T the temperature, A, B, C, D, E, a_{Gd}, b_{Gd} and c_{Gd} are adjustment constants and h_D is a function that takes into account the effects of burnup. On the other hand, the conductivity of all the Zry components [5] and the stainless-steel spring [67] are calculated with polynomial adjustment curves as a function of temperature.

DIONISIO can calculate the weight fraction of different gases (filling and/or due to fission in the fuel [68], [69]) in the free volume of the rod. These fractions are then used to calculate the conductivity of the total mixed gas in the plenum, according to a gas mixture law, which requires a weighted average conductivity for each gas as a function of the temperature (T) according to the exponential law [70]:

$$k = A_g \, T^{B_g} \tag{8}$$

where A_g and B_g are specific constants for each gas.

3.2 Boundary conditions

The boundary conditions of the problem are estimated from a thermo-hydraulic calculation of the cladding external temperature, the coolant temperature and the quality and velocity of the coolant. This calculation is done by sectors, as described in the Introduction, from which only the sector closest to the plenum is taken into account. As a user input value, the temperature distribution can be constant along the plenum sector of the core or it can follow a cosine law, in case there is a large temperature variation as is the case in accident conditions. For the latter, the cladding temperature in that sector (T_{sec}) is defined as the cladding boundary temperature in the lower area of the plenum domain, and, using said cosine form as a function of the height z, the boundary conditions of the rest of the domain take the form:

$$T_{bc}(z) = T_{sec} + \alpha_T \left(\cos\left(\frac{\pi z}{L_{ext}} \right) - 1 \right) \tag{9}$$

where L_{ext} is the extended length of the domain in the axial direction (typically 1.2 times the original length), and α_T is a variable that depends on the difference between T_{sec} and the outlet temperature of the coolant.

4. DIONISIO 3D Results

For the purpose of showing the behavior of the new version of DIONISIO, we selected a few experiments under irradiation with some particularities, to demonstrate the PCMI code response. These cases have been selected to prove the accuracy of our

model when compared to experiments and show that it performs better than or at least as good as previous 2D axisymmetric models. For future work, we plan to compare our code to experiments that do not present symmetric conditions and that cannot be simulated with models that are not three-dimensional. A few examples requiring three-dimensional domains include asymmetrical oblation of the cladding, asymmetrical heating conditions for the rod due to its position in the reactor core, superficial defects of the pellet produced in the assembly of the fuel elements, such as chips, and LOCA scenarios which involve ballooning of the cladding. In reference to the plenum model, we chose two experiments, one under normal operation and the other one for accident conditions, that show how the model works across the entire range of requirements.

4.1 The MOX experiments [71]:

The first set of experimental data used to compare the code results to, comes from the irradiation of the first Argentine prototypes of MOX fuels for PHWR reactors. They were built in the Alpha facility of CNEA and two of them, labeled A.1.2 and A.1.3, were irradiated in the high flux reactor of Petten, Holland, from January 1989 to October 1991. Both bars, consisting of 21 pellets, were submitted to a nearly constant power rate and rod A.1.3 was afterwards subjected to a power ramp [71]. The post irradiation examinations were performed at the Forschungszentrum, Karlsruhe, Germany in 1993 and included visual inspections. We have focused on rod A.1.3, being the most demanding in terms of rod behavior.

The most remarkable feature is the presence of ridges on the external surface of the cladding accompanying the pellets' distribution. A general radius increase can be seen, with the rod presenting a deformation of 0.55% at the belt. The effect is even more significant at the crests, where the deformation is of 1% approximately. Fig. 8 shows the average diameter of each of the five sectors the rod was divided into (with 4.2 pellets per sector), as it varies with the burnup, where sector 1 is the closest to the bottom and sector 5 is the closest to the top of the rod. The power history varies among the different sectors, with sector 5 being the one with highest linear power. The final values of each sector are in good correspondence with the ones provided by the experiments.

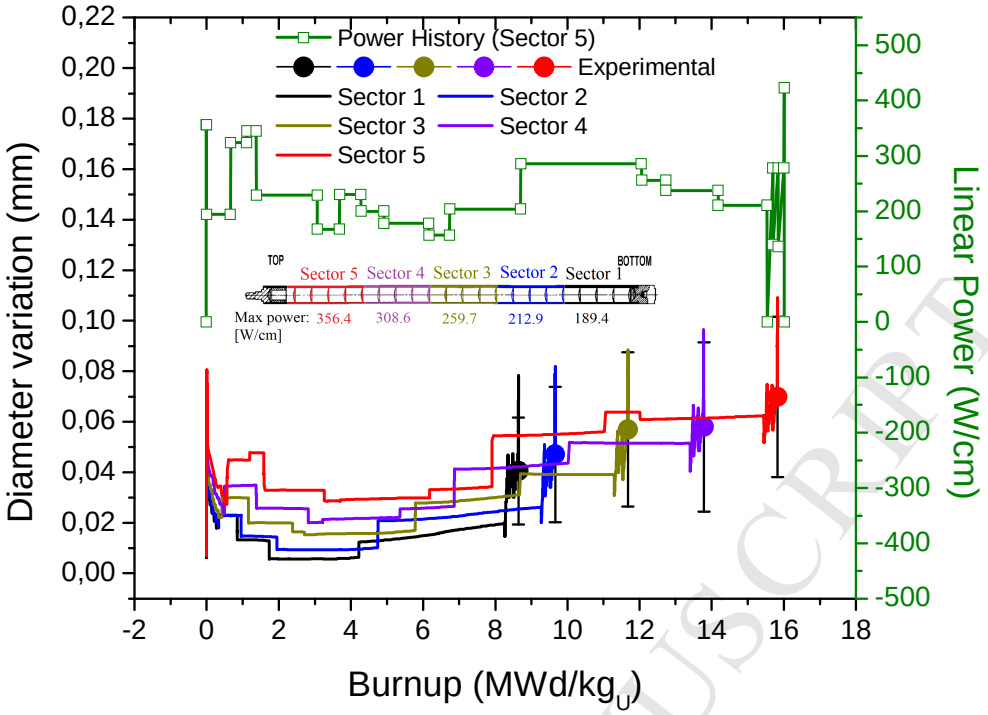

Fig. 8 Cladding outer diameter variation by axial sector through the burnup. Final experimental results overimposed at the end of each curve. Overimposed in green (vertical axis to the right) is the power history of sector 5, showing the final ramps. The image in the middle shows a scheme of the bar, the sectors and maximum power for each sector (prior to the final ramps).

In Fig. 9 the evolution of the central and superior radii of cladding are shown for sector 5 (highest burnup) and the entire rod average. In addition, the difference of this measures (the ridge) is compared to the experimental values at end of life for the A.1.3 rod. We observe a good coincidence of these results with the predicted ones.

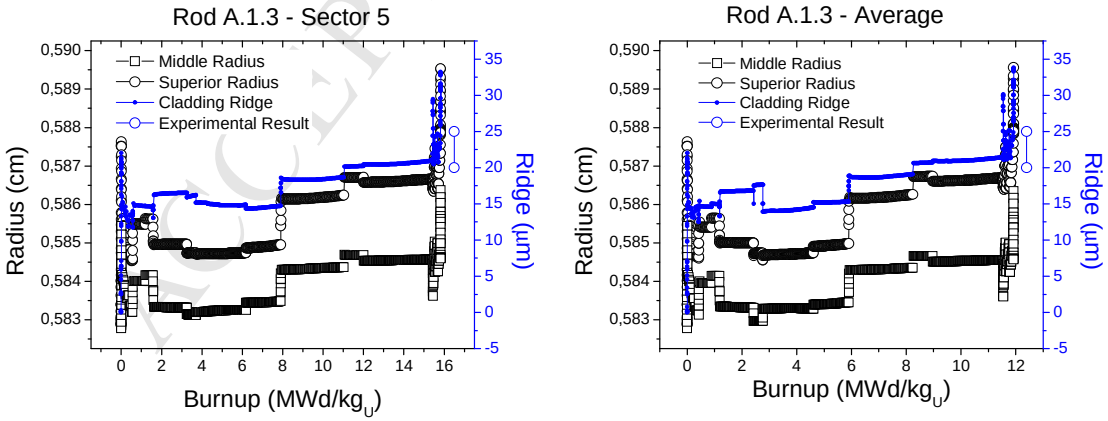

Fig. 9 Evolution of superior and middle radii and difference between them.
Left: sector 5 (highest burnup). Right: rod average.

In Fig. 10 we present the radial evolution of the contact surfaces (i.e. pellets and cladding inner radius) and hoop stress plotted as functions of the burnup to show the variation from increasing values when in contact to decreasing values when surfaces are

not pushing on each other. In said figure, some interpenetration can be noted mainly because both radii are averaged from the entire circumference, but on a closer inspection, values are below and up to 2 microns, which is to be expected (especially in a three-dimensional domain) given how the CZM performs the numerical solution for contact, as explained in section 2.2 of this paper.

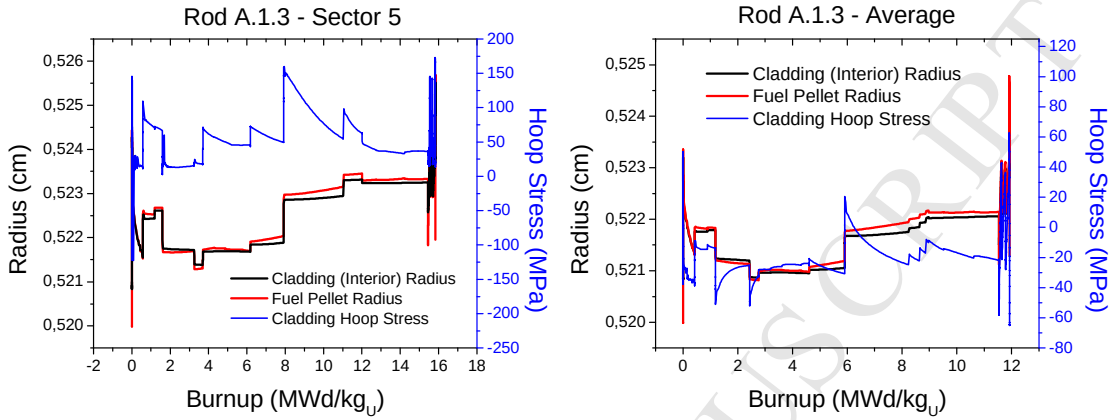

Fig. 10 Evolution of pellet and cladding inner radius (contact surfaces) and hoop stress. Left: sector 5 (highest burnup). Right: rod average.

4.2 The Contact Experiment [16], [17], [18]:

The CONTACT series of experiments used short rods of Zr-4 cladding UO_2 pellets of typical PWR 17x17 design. The purpose of the experiments was to improve the understanding of fuel rod performance. The rods were irradiated in a pressurized water loop at almost constant power. CONTACT 1 was irradiated at a constant power level close to 40 kW/m to a discharge burnup of ~22 MWd/kg$_U$. CONTACT 2 was irradiated at a constant power of ~25 kW/m and an internal helium pressure between 0.1-0.2 MPa. The rod was discharged early because of a failure at a burnup of ~5.5 MWd/kg$_U$ and replaced with the identical design rod CONTACT 2bis. CONTACT 2bis had a burnup of 12.4 MWd/kg$_U$. All the experiments were designed to analyze the performance of the fuels, and the cladding deformation was measured along other valuable results.

Measurement of cladding diameter for CONTACT 1 as a function of burnup showed an initial reduction due to creep down followed by a gradual expansion after fuel-to-cladding contact and closed gap. The evolution of diameter versus burnup for CONTACT 2bis showed an initial increase in diameter over the first 3 cycles of irradiation but there was not an explanation for this increase, as it is followed by a progressive decrease (by irradiation creep) to an equilibrium diameter of approximately 30 microns smaller than the initial.

In general, we can observe a higher power history in CONTACT 1, which leads to PCMI deforming the cladding with more intensity than CONTACT 2bis (Fig. 11). The numeric predictions of this experiment are in good correlation to the real values, which have a somewhat considerable dispersion.

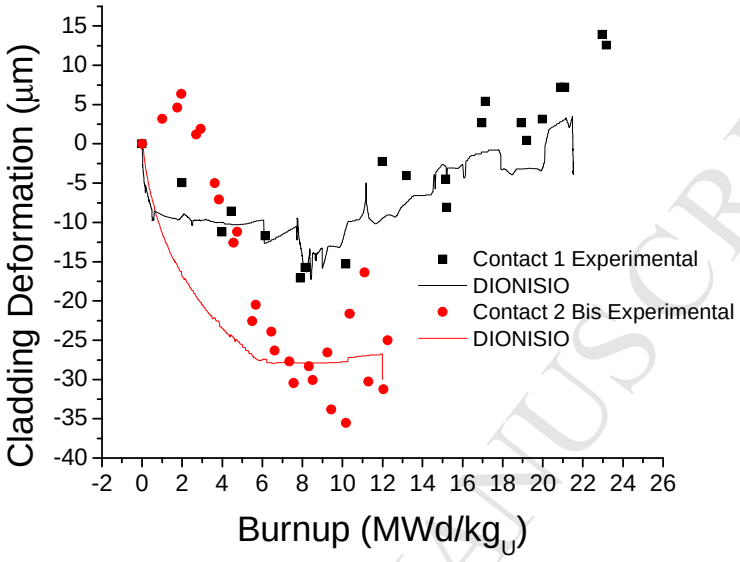

Fig. 11 Cladding deformation through burnup for Contact 1 and Contact 2bis.

Fig. 12 presents the radius of the cladding (internal) and pellet and the hoop stress as functions of the burnup. As in the case of the MOX experiments (section 4.1), in this figure, it is possible to see the increase in hoop stress when contact occurs. It is also possible to note that the hoop stress has a lower intensity than in the PHWR MOX experiments, which is to be expected since there are essentially different values of thermal requirements and design conditions of the fuel elements.

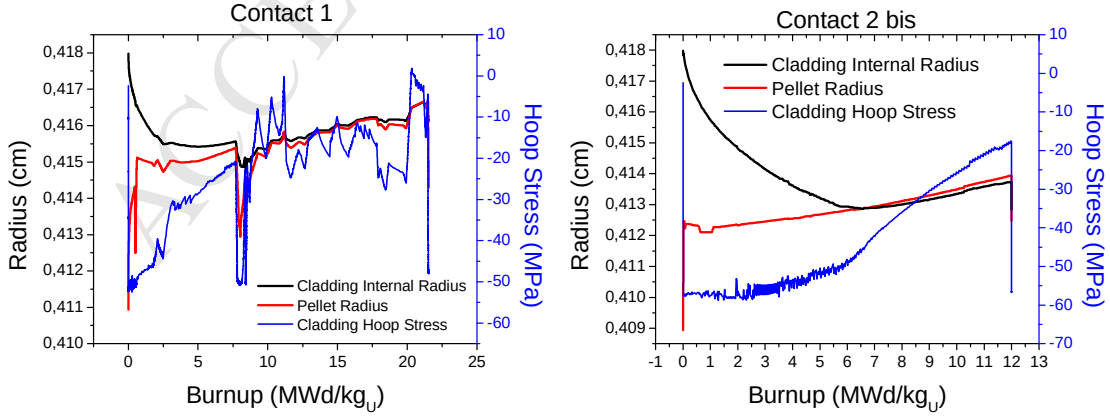

Fig. 12 Evolution of contact surfaces and hoop stress. Left: Contact 1. Right: Contact 2bis.

4.3 IRDMR Experiment (ABS, ACA):

The experiments referred to as IRDMR (In-Reactor Diameter Measuring RIG [72]) consisted of two cases, Exp-FIO-118 which comprised two single-element irradiations (ABS and ABH) and Exp-FIO-119, comprising five single-element irradiations (ACH, ACA, ACC, ACK and ACG). For our numerical simulations we have considered elements ABS which had the purpose of investigating the effect of fuel density on the fuel element dimensional response to power changes, and ACA, which was involved in a power ramp irradiation. The experiments were conducted at AECL's Chalk River Laboratories in the NRX PHWR between 1978 and 1983. The fuel elements were assembled using enriched (3.5 wt% U-235 in U) UO_2 fuel pellets and a Zr-4 cladding, with a coating of graphite over the inner surface of the sheath. Diametral changes of single fuel elements were measured while at power. Both elements had irradiation histories consisting of several steps detailed in the experiment.

In Fig. 13 it can be observed that diameter and ridge calculations are in good correlation with experimental measurements, as they increase and decrease with each power ramp. In addition to being pre-irradiated at a power of 30 kW/m, the ACA element was irradiated with a lower ramp rate than ABS, and it can be seen on the right of the figure that it presents a lower ridge.

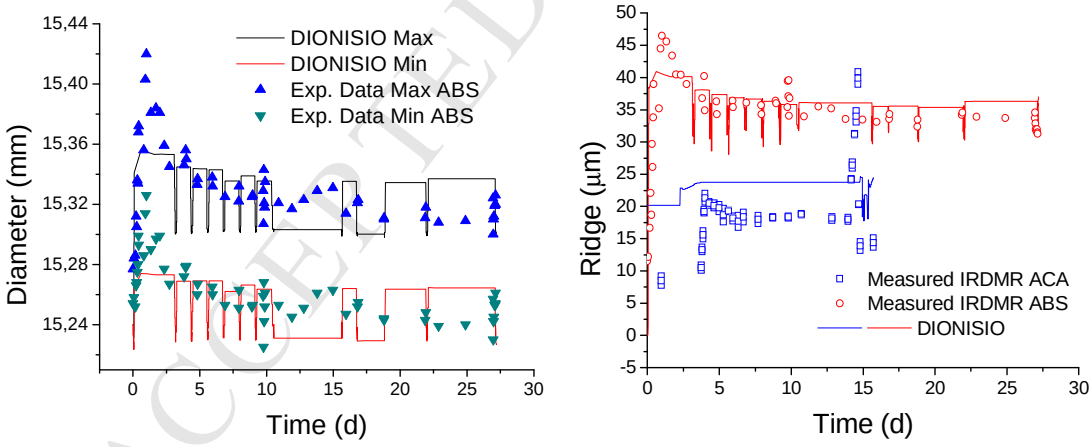

Fig. 13 Left: calculated and measured maximum and minimum diameter for ABS element through irradiation time. Right: calculated and measured ridge for ABS and ACA elements through time.

In Fig. 14 we show colormaps of the domain at the last ramp of the ABS experiment, when performing a simulation with double-case (two half-pellets). On the left, the Von Mises stress distribution can be seen with a maximum in the middle of the pellets and decreasing along the axial and radial directions. The values reached are quite high since the model does not account for microcracks or creep in the pellet. However,

it does include a viscoplastic term that leads to stress relaxation in time. Additionally, radial displacements have been increased 25 times for them be easier to see, which allows us to show the bamboo effect on the cladding over both pellets. On the right, a temperature profile can be seen where the highest temperature lies in the center of the stack and decreases radially.

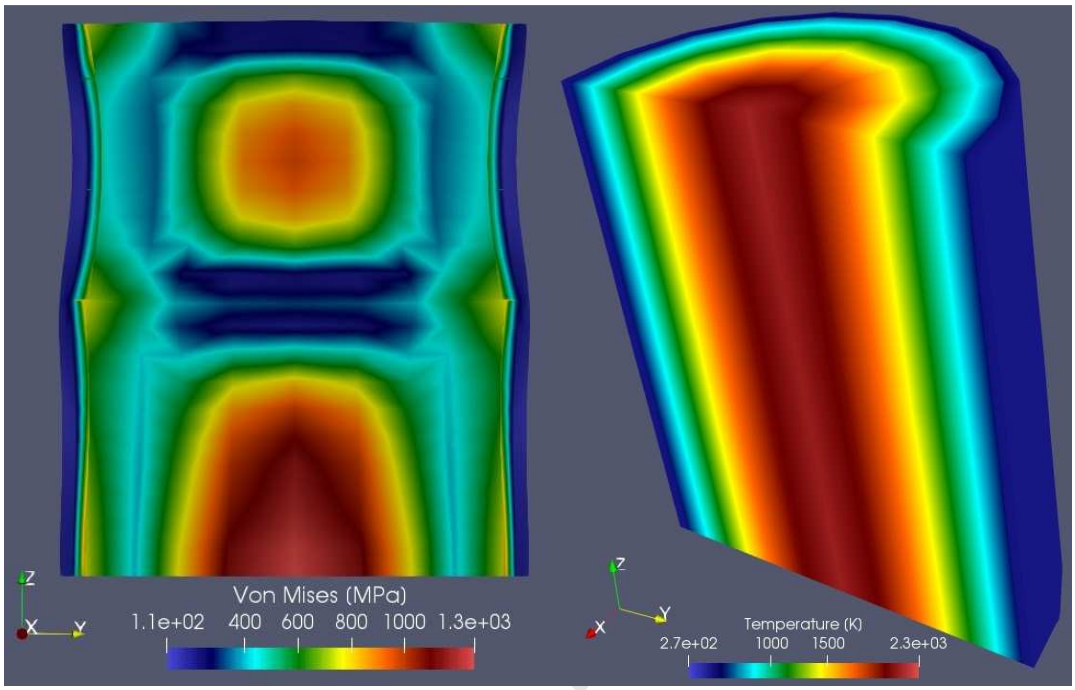

Fig. 14 ABS domain colormap at the last power ramp, showing two half-pellets and cladding. Left: Von Mises stress (radial displacements x25). Rigth: temperature.

4.4 OSIRIS Experiment (G07, H09)

The Osiris experiments consisted of 4 PWR EDF/FRAMATOME/CEA rods irradiated in EDF commercial reactors. Two of these rods, identified as G07 [73] and H09 [74], were irradiated in the EDF Graveline 3 PWR for 864 days and the EDF Cruas 2 PWR for 1182 days, respectively and different parameters were measured, including the temperature of the cladding. For practical purposes we consider the cladding temperature equal to the plenum temperature.

Fig. 15 shows the plenum temperature for the 2D and 3D simulations and the linear power as functions of time for rods G07 and H09. Fig. 15 shows a good fit between the calculated and experimental temperatures, with a difference of around 2% with respect to the measured values, except for the first four points, for which this difference is closer to 4%. For rod H09, Fig. 15b shows a difference of less than 2% with respect to the experimental temperature. Both graphs show that the results for two and three dimensions overlap.

The inset images in Fig. 15 show the evolution of the plenum temperature as the power history and time for the experiments progresses. It can be seen that the pellet and plenum temperature increase gradually, product of the rarefaction of the internal atmosphere due to the increase in temperature of the pellet. In the inset image of Fig. 15a, it can be noted that the first four images (top to bottom) correspond to the temperature during the power ramp at the beginning. From the fifth image (7 days) onward, the distribution reaches the stationary level. At around 125 days, a slight increase in the pellet central temperature is observed due to the modification of its conductivity as a consequence of burnup among other factors. In the images corresponding to 400 and 600 days, increases in both plenum and pellet central temperatures are observed due to slight increases in the operating power and a variation in the pellet and plenum conductivity. In the last image (600 days), the highest temperature reached in the whole experiment is observed in the pellet center. A similar behavior can be followed for the OSIRIS H09 experiment in the inset of Fig. 15b.

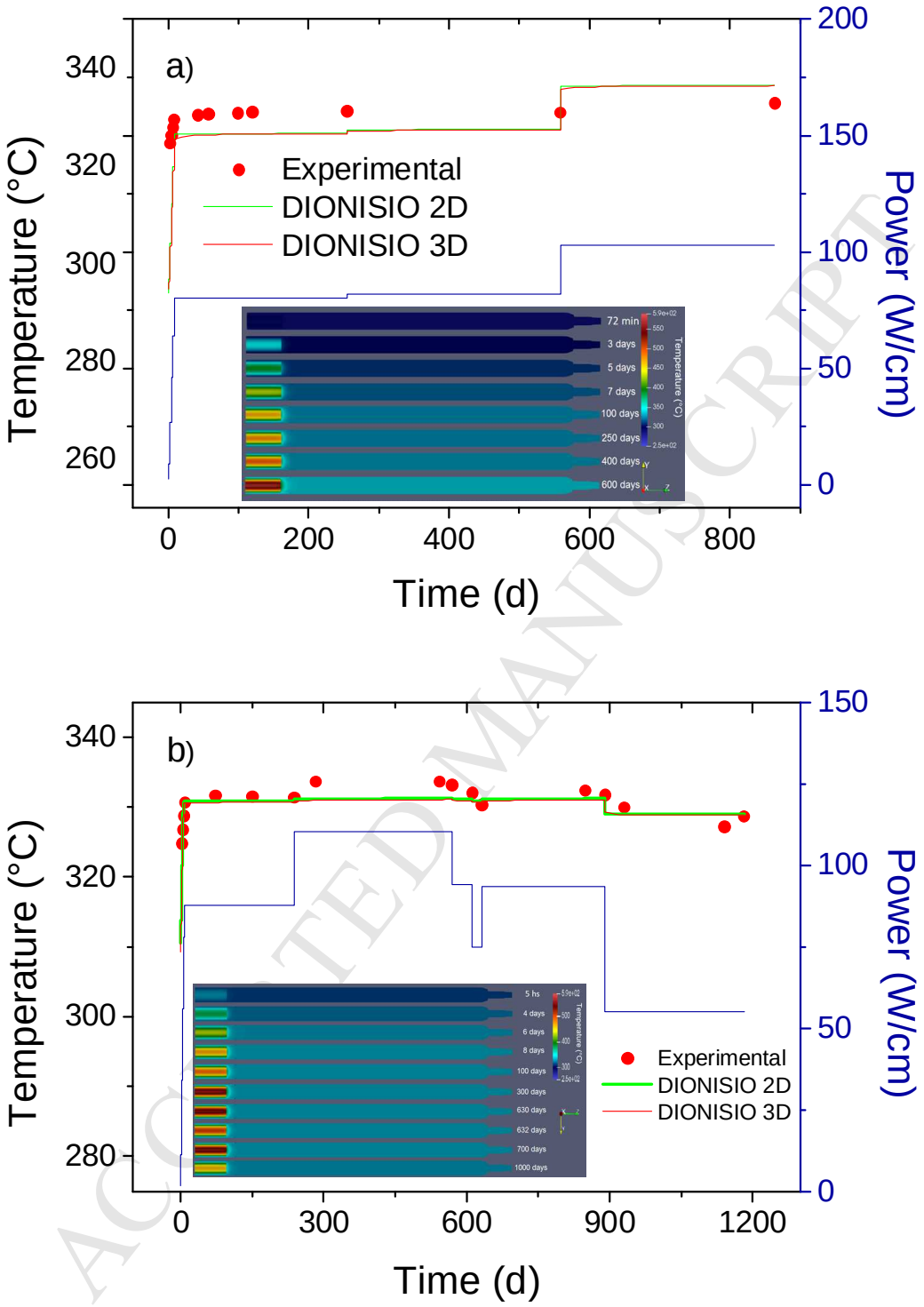

Fig. 15 Plenum temperature and lineal power as functions of time (in days). Inset images of evolution of calculated temperature in the fuel rod plenum. a) rod G07; b) rod H09.

4.5 IFA-650.1 and .2 Experiment:

The IFA-650 (Instrumented Fuel Assembly, 650 series) experiments had the objective of analyzing safety criteria for LOCA accidents. New designs and materials as well as an inclination to burnup extension regulated the necessity of suitable

measurements. These tests were comprehensive in-pile studies under emulated LOCA conditions, such as abrupt pressure drop and low coolant flow. Thermo-physical and thermo-chemical aspects like relocation of the fragmented pellet, cladding temperature, ballooning, cladding hydriding and oxidation were examined. All of this was performed at the Halden Reactor (Norway), using fuel rods which had been irradiated in commercial PWR or BWR reactors reaching intermediate or high burnup [75].

In these tests, a rod was located in the center of an insulated standard high-pressure flask, which was connected to a high-pressure heavy water loop and a blow-down system. The fuel rod was surrounded by a heated flow separator and the flask. The rods were 50 cm long with an external diameter of 9.5 mm, composed of a Zr-4 cladding 0.57 mm thick containing UO_2 pellets. The difference between both experiments lies primarily in the base irradiation histories, the rate of pressure and coolant mass flow drop, the thermocouples location and the filling pressure of He (2 and 40 bar, respectively) [76]-[78].

These experiments were used to compare cladding temperature and internal pressure to DIONISIO accident subroutines for LOCA conditions, published in reference [75]. In this paper, we focus solely on the results for the plenum temperature while fully simulating the accident conditions. It should be highlighted that in the experiment, the plenum temperature was not measured explicitly. We compare to the outlet temperature of the coolant, with the plenum temperature expected to be a little higher due to its proximity to the source of power and heat.

4.5.1 IFA-650.1

In the IFA-650.1, linear power presents plateau periods and increments by stepped jumps between those plateaus. Six pressure drops followed by stationary periods take place in between. No burst occurs during the experiment.

Fig. 16 presents the comparison between plenum temperature obtained with DIONISIO in green and the coolant outlet temperature (TOA, temperature at outlet in average) in red, along with power and pressure histories of the experiment. In general, the difference in temperature values does not exceed 8% except for the last pressure drop, where it is close to 15%.

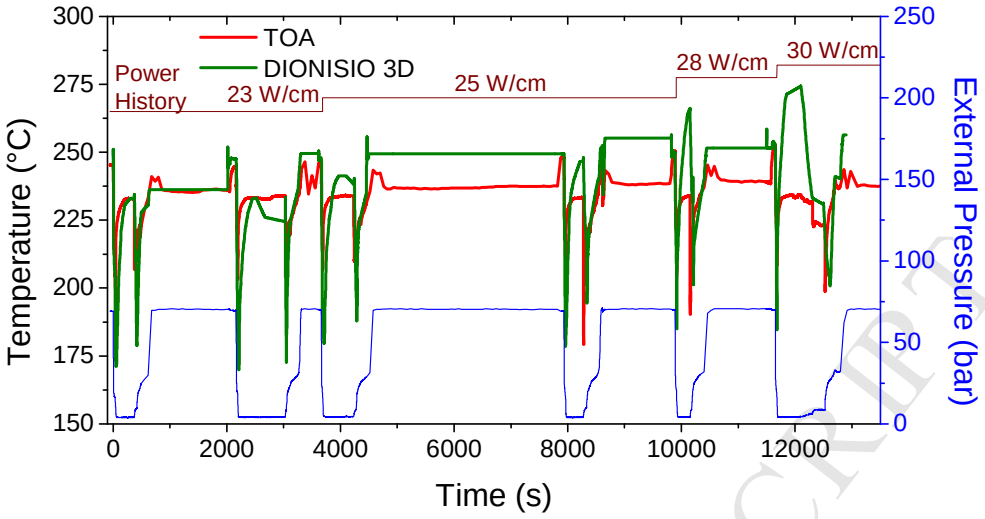

Fig. 16 IFA-650.1 measured coolant outlet temperature and calculated plenum temperature.

4.5.2 IFA-650.2

This experiment consists in subjecting a fuel rod to a pressure of about 70 bars and a linear power of 23.5 W/cm. While power stays constant, coolant pressure decreases suddenly to simulate accident conditions. After 450 seconds, when scram happens, power diminishes to almost zero.

In Fig. 17, plenum temperature evolution calculated with DIONISIO is observed and compared to coolant outlet average temperature (TOA) of IFA-650.2 experiment. During the first 40 seconds of the accident, plenum temperature decreases progressively towards 165 °C. This is due to an increase in heat removal produced by the nucleation of boiling bubbles. As time progresses, temperature increases up to 265 °C. Finally, after scram, a final plenum temperature decrease is observed, as can also be seen in the inset of Fig. 17.

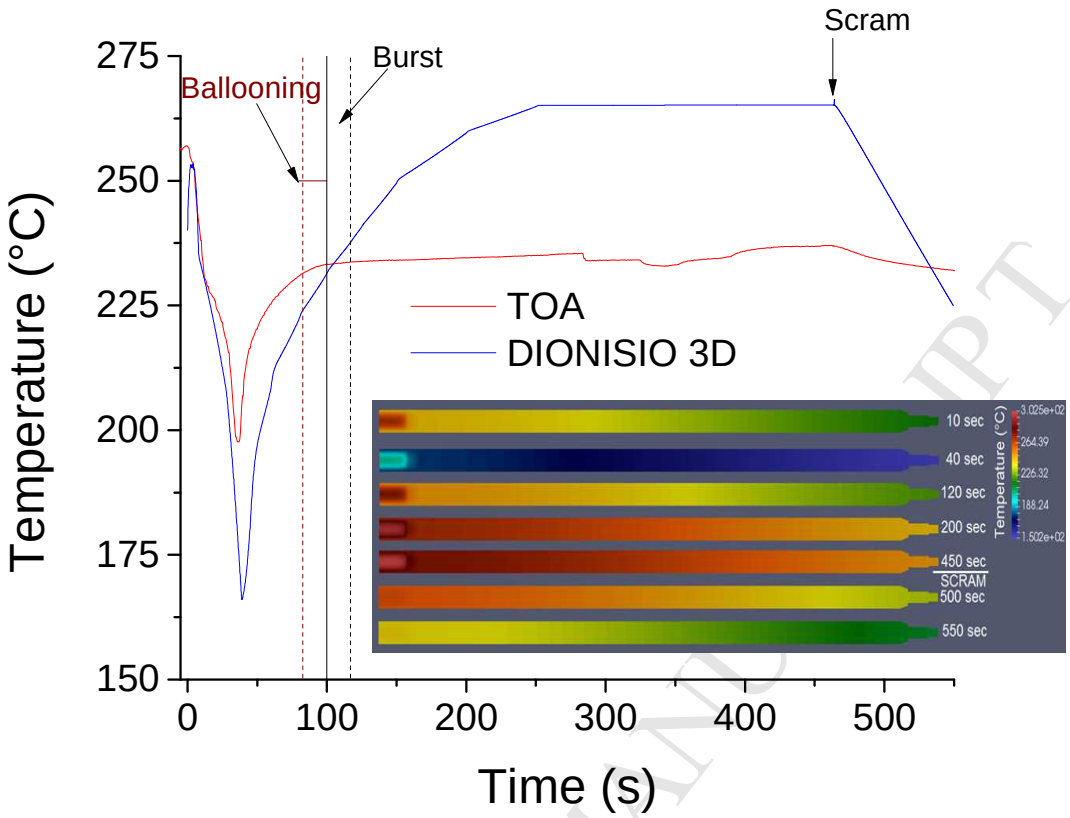

Fig. 17 IFA-650.2 measured coolant outlet temperature and calculated plenum temperature. Inset image of evolution of calculated plenum temperature over time.

5. Conclusions

The new version of DIONISIO, iteration 3.0, has incorporated full 3D models in the pellet-gap-cladding domain by sector and in the plenum domain. For the first one, we needed to develop a new contact algorithm based in Cohesive Zone methods, a framework included in FEM concepts, developed initially to treat fracture mechanics and problems involving cracks. Despite the limitations discussed at the end of section 2.2, this new contact algorithm shows a better performance in comparison to previously implemented methods regarding scenarios from problems from the literature that have analytical solution. Furthermore, we compared the recently incorporated algorithms to experimental tests developed to emulate PCMI with a very good correlation. The use of the algorithm inside the code, considering irradiation and the interplay with the other models included in DIONISIO, exhibits an acceptable performance in the prediction of "bamboo effects" and radial cladding deformation. We show here just a few results in selected experiments such as CNEA-MOX rod experiments, the Contact Experiment and IRDMR experiments.

The plenum model shows an acceptable behavior in all the tested experimental ranges, described in the results we have presented. The OSIRIS and IFA-650 experimental series let us use the model in a wide assortment of situations showing very good results with errors in temperature between 10-15% in the cases with the largest variation. It is worth noting that this model does not yet take into account heat radiation, even though its contribution is below the order of 1.4% than the energy delivered to the free volume of the plenum by thermal conduction.

In a future publication we will present the general behavior of DIONISIO 3.0, showing the integral performance of the code against complete sets of experimental data to which we have access, so as to validate the complete code in its full three-dimensional version.

Acknowledgments

E. Goldberg and M. E. Loza Peralta have scholarships from Comisión Nacional de Energía Atómica.

A. Soba is a researcher at the Consejo Nacional de Investigaciones Científicas y Técnicas (CONICET).

We thank Eng. M. E. Cazado for providing the rod designs used in Fig. 1.

References

[1] A. Soba, A. Denis, DIONISIO 2.0: New version of the code for simulating a whole nuclear fuel rod under extended irradiation, Nuclear Engineering and Design 292 (2015).

[2] A. Soba, A. Denis, L. Romero, E. Villarino, F. Sardella, A high burnup model developed for the DIONISIO code, Journal of Nuclear Materials, Vol. 433, Issues 1-3 (2013).

[3] A. Soba, M. Lemes, A. Denis, An empirical formulation to describe the evolution of the high burnup structure, Journal of Nuclear Materials, 456 (2015).

[4] A. Soba, M. Lemes, M. E. González, A. Denis, L. Romero, Simulation of the behaviour of nuclear fuel under high burnup conditions, Annals of Nuclear Energy 70 (2014).

[5] A. Soba, Simulación del comportamiento termomecánico de una barra combustible en operación. Doctoral thesis, FCEyN, UBA, (2007).

[6] A. Soba and A. Denis, Simulation with Dionisio 1.0 of thermal and mechanical pellet-cladding interaction in nuclear fuel rods. J. of Nucl. Mater. 374 (2008).

[7] A. Denis, R. Piotrkowski, Simulation of isothermal fission gas release, Journal of Nuclear Materials 229 5,6 (1996).

[8] B.J. Lewis, F.C. Iglesias, R.S. Dickson, A. Williams. Overview of high-temperature fuel behaviour with relevance to CANDU fuel. Journal of Nuclear Materials 394 (2009).

[9] Shane Stimpsona, Jeffrey Powers, Kevin Clarno, Roger Pawlowski, Russell Gardner, Stephen Novascone, Kyle Gamble, Richard Williamson. Pellet-clad mechanical interaction screening using VERA applied to Watts Bar Unit 1, Cycles 1–3Nuclear Engineering and Design 327 (2018).

[10] L.E. Herranz, I. Vallejo, G. Khvostov, J. Sercombe, G. Zhou. Assessment of fuel rod performance codes under ramp scenarios investigated within the SCIP Project, Nuclear Engineering and Design 241 (2011).

[11] Motoe Suzuki, Hiroshi Uetsuka, Hiroaki Saitou. Analysis of mechanical load on cladding induced by fuel swelling during power ramp in high burnup rod by fuel performance code FEMAXI-6, Nuclear Engineering and Design 229 (2004).
[12] K. Yueh, J. Karlsson, J. Stjarnsater, D. Schrire, G. Ledergerber, C. Munoz-Reja, L. Hallstadius. Fuel cladding behavior under rapid loading conditions. Journal of Nuclear Materials 469 (2016).
[13] J. Mathews, The quantitative description of deformation and stress in cylindrical fast reactor fuel pins, in Advances in Nuclear Science and Technology, Vol.6 (1972), Academic Press.
[14] L. Caillot, B. Linet, C. Lemaignan, Pellet clad interaction in PWR fuel. Analytical irradiation experiment and finite element modelling, (Proc. SMIRT 12, Stuttgart, Germany, 1993).
[15] Simulation of Pellet-Cladding Thermomechanical Interaction and Fission Gas Release. A. Denis and A. Soba. Nuclear Engineering and Design 223 (2003).
[16] IFPE/CONTACT REV.1. DATABASE FOR CONTACT EXPERIMENTS IRRADIATED AT CEA GRENOBLE. J A TURNBULL October 1998 Revision 1 issued Jan 2003 following comments by D Elenkov.
[17] M. Bruet, J. Dodalier, P. Melin and M. L. Pointud: "CONTACT 1 and 2 Experiments: Behaviour of PWR Fuel Rods up to 15000 MWd/t" IAEA Specialists' Meeting on Water Reactor Fuel Elements Performance Computer Modelling, Blackpool, UK, 17-21 March 1980.
[18] M. Charles and C. Lemaignan: "Fuel Performance under Normal PWR Conditions: A Review of Relevant Experimental Results and Models", J. Nucl. Mater. vol. 188, 1992.
[19] Kinoshita and Ichikawa. “Analysis of fuel rod deformation”. Nucl. Eng. and Des. 56 (1980).
[20] J. Desquines, D. A. Koss, A. T. Motta, B. Cazalis, M. Petit. The issue of stress state during mechanical tests to assess cladding performance during a reactivity-initiated accident (RIA) Journal of Nuclear Materials 412 (2011).
[21] B. Cazalis, J. Desquines, S. Carassou, T. Le Jolu, C. Bernaudat. The plane strain tests in the PROMETRA program. Journal of Nuclear Materials 472 (2016).
[22] Luis Alva, Kirill Shapovalov, George M. Jacobsen, Christina A. Back, Xinyu Huang. Experimental study of thermo-mechanical behavior of SiC composite tubing under high temperature gradient using solid surrogate. Journal of Nuclear Materials 466 (2015).
[23] Sun-Ki Kim, Je-Geon Bang, Dae-Ho Kim, Ik-Sung Lim, Yong-Sik Yang, Kun-Woo Song, Do-Sik KimHoop strength and ductility evaluation of irradiated fuel cladding. Nuclear Engineering and Design 239 (2009).
[24] I. C. Sagrado, L.E. Herranz. Modeling RIA benchmark cases with FRAPTRAN and SCANAIR: A comparative exercise. Nuclear Engineering and Design 278 (2014).
[25] Tanweer Alam, Mohd. Kaleem Khan, Manabendra Pathaka, K. Ravib, Ritu Singhb, S.K. Guptab. A review on the clad failure studies. Nuclear Engineering and Design 241 (2011).
[26] John C. Luxat, David R. Novog. A generalized failure map for fuel elements subject to a power pulse. Nuclear Engineering and Design 241 (2011).
[27] Arthur Hellouin de Menibus, Jerome Sercombe, Quentin Auzoux, Christophe Poussard. Thermomechanical loading applied on the cladding tube during the pellet cladding mechanical interaction phase of a rapid reactivity initiated accident. Journal of Nuclear Materials 453 (2014).
[28] Kurt A. Terrani. Accident tolerant fuel cladding development: Promise, status, and challenges. Journal of Nuclear Materials 501 (2018).
[29] M. Ben-Belgacem, V. Richet, K. A. Terrani, Y. Katoh, L.L. Snead. Thermo-mechanical analysis of LWR SiC/SiC composite cladding. Journal of Nuclear Materials 447 (2014).
[30] K. Lassmann, TRANSURANUS: a fuel rod analysis code ready for use, J. Nucl. Mater., 188 (1992).
[31] A. C. Marino, E. J. Savino, S. Harriague, BACO (Barra Combustible) code version 2.20: a thermo-mechanical description of a nuclear fuel rod, J. Nucl. Mater., 229 (2) (1996) 155-168.

[32] I. Palmer, G. Rossiter, R. White, Development and validation of the ENIGMA code for MOX fuel performance modelling, MOX Fuel Cycle Technologies for Medium and Long Term Deployment, IAEA/OECD Symposium, Vienna, (2000).
[33] K. Geelhood, W. Luscher, C. Beyer, M. Flanagan, FRAPCON-3.4: a computer code for the calculation of steady-state, thermal-mechanical behavior of oxide fuel rods for high burnup, NUREG/CR-7022 (1) (2011).
[34] Alain Moal, Vincent Georgenthum, Olivier Marchand. Institut SCANAIR: A transient fuel performance code, Part One: General modelling description. Nuclear Engineering and Design 280 (2014).
[35] Jin-Sik Cheon, Byung-Ho Lee, Yang-Hyun Koo, Je-Yong Oh, Dong-Seong Sohn, Evaluation of a pellet-clad mechanical interaction in mixed oxide fuels during power transients by using axisymmetric finite element modeling Nuclear Engineering and Design 231 (2004).
[36] M. Suzuki, H. Saitou, Y. Udagawa, F. Nagase, Light Water Reactor Fuel Analysis Code FEMAXI-7; Model and Structure, JAEA-Data/Code 2013-005.
[37] A. Zangari, R. Montgomery, Fuel analysis and licensing code: FALCON MOD01, Volume 2: User's Manual, Technical Report EPRI 1011308 (2004).
[38] B. Linet, X. Suo, The METEOR/TOUTATIS code A 2D/3D code for fuel behaviour simulation, Canadian Nuclear Society/American Nuclear Society 4th international conference on simulation methods in nuclear engineering, (p. 2v), Canada (1993).
[39] B. Baurens, J. Sercombe, C. Riglet-Martial, L. Desgranges, L. Trotignon, P. Maugis, 3D thermo-chemical–mechanical simulation of power ramps with ALCYONE fuel code, J.Nucl.Mater. 452 (2014) 578–594.
[40] Hyo Chan Kim, Sang Kyu Seo, Sung Uk Lee, Yong Sik Yang. Development of NUFORM3D module with FRAPCON3.4 for simulation of pellet-cladding mechanical interaction Nuclear Engineering and Design 318 (2017).
[41] Nathan Capps, Michael Kennard, Wenfeng Liu, Brian D. Wirth, Joe Rashid. PCI analysis of a commercial PWR using BISON fuel performance code Nuclear Engineering and Design 324 (2017).
[42] R. Radovitzky, A. Seagraves, M. Tupek, L. Noels. *A scalable 3D fracture and fragmentation algorithm based on a hybrid, discontinuous Galerkin, cohesive element method.* Comput. Methods Appl. Mech. Engrg. 200 (2011).
[43] L. Noels, R. Radovitzky. *An explicit discontinuous Galerkin method for non-linear solid dynamics: Formulation, parallel implementation and scalability properties.* Int. J. Numer. Meth. Engng; 74:1393–1420 (2008).
[44] Francisco J. Gallego y Juan J. Anza, "Un modelo de elementos finitos mixtos para la resolución del problema del contacto elástico", Métodos numéricos para cálculo y diseño en ingeniería, vol5, 2, 163-184 (1989).
[45] Ulf Sellgren, Stefan Björklund, Sören Andersson, "A finite element-based model of normal contact between rough surfaces", Wear 254 1180,1188 (2003).
[46] J. Zurita, M. Doblare y L. Garcia, "Determinación de tensiones de contacto mediante el M.E.C. en problema multicuerpo con simetría axial", Métodos numéricos para cálculo y diseño en ingeniería, vol 9, 1, 15-34 (1993).
[47] Klaus-Jürgen Bathe and Anil Chaudhary, "A solution method for planar and axisymmetric contact problems", Int. J. Num. Meth. Engng,21,65-88 (1985).
[48] Klaus-Jürgen Bathe, Finite Element Procedures, PRENTICE HALL, 1996.
[49] Barenblatt, G. I. *The mathematical theory of equilibrium cracks in brittle fracture*. Advances in applied mechanics, 7, (1962).
[50] Dugdale D.S. *Yielding of Steel Sheets Containing Slits*. Journal of the Mechanics and Physics of Solids 8, 1960.
[51] Rice J.R. *Mathematical analysis in the mechanics of fracture*. Fracture: An Advanced Treaties 2, (1968).
[52] Xu, X. P., & Needleman, A. Numerical simulations of fast crack growth in brittle solids. *Journal of the Mechanics and Physics of Solids*, *42*(9), (1994).
[53] Contact, adhesion and rupture of elastic solids. D. Maugis. Springer (2000).

[54] Problemas de Resistencia de materiales. Miroliubov, L., Engálichev, S., Serguiévski, N., Almamétov, F., Kúritsin, N., Smirnov-Vasíliev K., Yáshina L., Es. Mir, (1975).
[55] Hunter, S. C. (1960). The Hertz problem for a rigid spherical indenter and a viscoelastic half-space. *Journal of the Mechanics and Physics of Solids*, *8*(4), 219-234.
[56] L. J. Segerlind, Applied finite element analysis, 2nd Ed., Wiley (1984).
[57] J. Planas, M. Elices, G. V. Guinea, F.J. Gómez, D. A. Cendon, I. Arbilla Generalizations and specializations of cohesive crack models. Engineering Fracture Mechanics 70 (2003).
[58] V. Tvergaard, A. Needleman. Effects of nonlocal damage in porous plastic solids. Int J. Solids Struct., 32(8/9), (1995).
[59] L. Noels, R. Radovitzky. A general discontinuous Galerkin method for finite hyperelasticity. Formulation and numerical applications. Int. J. Numer. Meth. Engng ; 68:64–97 (2006).
[60] R. Radovitzky, A. Seagraves, M. Tupek, L. Noels. A scalable 3D fracture and fragmentation algorithm based on a hybrid, discontinuous Galerkin, cohesive element method. Comput. Methods Appl. Mech. Engrg. 200 (2011).
[61] Tayyebe Seif. *DUCTILE FRACTURE ANALYSIS IN A STEEL PLATE BY COHESIVE ZONE MODELING*, Master thesis, (2014).
[62] Fehmi Cirak, Michael Ortiz, Anna Pandolfi. *A Cohesive Approach to Thin-Shell Fracture and Fragmentation*. Computer Methods Applied Mechanics and Engineering Comput, 194 (21-24), (2005).
[63] Park, K. C. (1982). A family of solution algorithms for nonlinear structural analysis based on relaxation equations. *International Journal for Numerical Methods in Engineering*, *18*(9), 1337-1347.
[64] da Silva, D. M. L., Jacob, B. P., & Rodrigues, M. V. (2006, January). Implicit and explicit implementation of the dynamic relaxation method for the definition of initial equilibrium configurations of flexible lines. In *25th International Conference on Offshore Mechanics and Arctic Engineering* (pp. 131-140). American Society of Mechanical Engineers.
[65] Hughes, Thomas JR. "Linear static and dynamic finite element analysis." *The Finite Element Method* (1987).
[66] M. E. González, A. Soba, y A. Denis, "Modelización de la conductividad térmica del UO2 y (U,Gd)O2 bajo irradiación. Implementación en el código DIONISIO", ANALES AFA, vol. 25, n.o 4, nov. 2014.
[67] IAEA THERPRO: "Thermo-Physical Material's Properties Database". Available in: http://therpro.hanyang.ac.kr/search/plot.jsp?symbol=Fe%2CCr%2CNi%2CX&prop=THC&submit_list=%3D-%3DSMSTST14THC198302&btn=close&.
[68] H. Bailly, C. Prunier, y D. Ménessier, The Nuclear Fuel of Pressurized Water Reactors and Fast Neutron Reactors: Design and Behaviour. Intercept Limited, 1999.
[69] D. R. Olander, Fundamental Aspects of Nuclear Reactor Fuel Elements. EEUU: Technical Information Center, Office of Public Affairs Energy Research and Development Administration, 1976.
[70] C. M. Allison, MATPRO, A Library of Materials Properties for Light-Water-Reactor Accident Analysis, vol. IV. 1993.
[71] A. Marino, E. Pérez, P. Adelfang, *Irradiation of Argentine (U,Pu)O_2 MOx fuels. Postirradiation results and experimental analysis with the BACO code*, J.Nucl. Mater. 229 (1996) 169-186.
[72] NEA-1777 IFPE/CANDU-IRDMR. (2007).
[73] "Rapport d'assurance qualite crayon FF06E2BV/G07/1067", CEA, France, oct. 1998.
[74] "Rapport d'assurance qualite crayon FF0EFELX/H09/5007", CEA, France, oct. 1998.
[75] M. Lemes, A. Soba, H. Daverio, y A. Denis, "Inclusion of models to describe severe accident conditions in the fuel simulation code DIONISIO", *Nuclear Engineering and Design*, vol. 315, pp. 1-10, abr. 2017.
[76] V. Lestinen, E. Kolstad, W. Wiesenack, LOCA testing at Halden, Trial runs in IFA-650, Nuclear Safety Research Conference Washington, (2003).

[77] V. Lestinen, LOCA testing at Halden, first experiment IFA-650.1 HWR-762, (2004).
[78] M. Ek, LOCA testing at Halden; the second experiment IFA-650.2, HWR-813, (2005).